Science AAAS

14 March 2017

Title: Femtosecond electron-phonon lock-in via photoemission and x-ray free-electron laser

Authors: S. Gerber[1,2†], S.-L. Yang[1,3†], D. Zhu[4], H. Soifer[1], J. A. Sobota[1,5], S. Rebec[1,3], J. J. Lee[1,3], T. Jia[1,3], B. Moritz[1], C. Jia[1], A. Gauthier[1,3], Y. Li[1], D. Leuenberger[1], Y. Zhang[6], L. Chaix[1], W. Li[1], H. Jang[7], J.-S. Lee[7], M. Yi[8], G. L. Dakovski[4], S. Song[4], J. M. Glownia[4], S. Nelson[4], K. W. Kim[9], Y.-D. Chuang[5], Z. Hussain[5], R. G. Moore[1], T. P. Devereaux[1], W.-S. Lee[1*], P. S. Kirchmann[1*], Z.-X. Shen[1,3*]

Affiliations:

[1]Stanford Institute for Materials and Energy Sciences, SLAC National Accelerator Laboratory and Stanford University, Menlo Park, CA 94025, USA.

[2]SwissFEL and Laboratory for Micro and Nanotechnology, Paul Scherrer Institut, 5232 Villigen PSI, Switzerland.

[3]Geballe Laboratory for Advanced Materials, Departments of Physics and Applied Physics, Stanford University, Stanford, CA 94305, USA.

[4]Linac Coherent Light Source, SLAC National Accelerator Laboratory, Menlo Park, CA 94025, USA.

[5]Advanced Light Source, Lawrence Berkeley National Laboratory, Berkeley, CA 94720, USA.

[6]International Center for Quantum Materials, Peking University, Beijing 100871, China.

[7]Stanford Synchrotron Radiation Lightsource, SLAC National Accelerator Laboratory, Menlo Park, CA 94025, USA.

[8]Department of Physics, University of California Berkeley, Berkeley, CA 94720, USA.

[9]Department of Physics, Chungbuk National University, Cheongju 28644, Korea.

[†]These authors contributed equally to this work.

[*]Correspondence to: kirchman@stanford.edu, leews@stanford.edu, zxshen@stanford.edu

Abstract: The interactions that lead to emergence of superconductivity in iron-based materials remain a subject of debate. It has been suggested that electron-electron correlations enhance electron-phonon coupling in FeSe and related pnictides, but direct experimental verification is lacking. Here, we quantify the electron-phonon coupling strength in FeSe by combining two time-domain experiments into a 'coherent lock-in' measurement in the THz regime. X-ray diffraction tracks the light-induced femtosecond coherent lattice motion at a single phonon frequency, and photoemission monitors the subsequent coherent changes in the electronic band structure. Comparison with theory reveals a strong enhancement of the coupling strength in FeSe owing to correlation effects. As the electron-phonon coupling impacts superconductivity exponentially, this enhancement highlights the importance of the cooperative interplay between electron-electron and electron-phonon interactions.

Main Text: Many of the rich properties of complex materials, such as the iron-based pnictides and chalcogenides (*1*), arise from a coupling of charge, orbital, spin and lattice degrees of freedom. For example, the cooperative interplay of electron-phonon (EP) and electron-electron interactions has been suspected to play an important role in unconventional superconductors (*2–5*) even though the physics is clearly beyond the canonical Bardeen-Cooper-Schrieffer theory (*6*). Although the EP coupling strength can be inferred from various spectroscopies (*7,8*), they rely on non-trivial assumptions and modeling. Ultrafast techniques, especially femtosecond time- and angle-resolved photoemission spectroscopy (trARPES) (*9*) and x-ray diffraction (trXRD) (*10*), bolstered by the advent of x-ray free-electron lasers (*11*), now open a window of opportunity for direct measurements of the EP coupling strength with sufficient precision to quantitatively test theories. Here, we combine these two techniques to link electronic and lattice

degrees of freedom, and determine the EP coupling strength directly and purely from experiments.

The EP coupling strength can be quantified by the deformation potential, defined as the ratio of a band energy shift to the corresponding atomic displacement (*12*). Experimentally, atoms can be displaced by initiating a coherent phonon mode via photo-excitation of the electrons (*13*). The light-induced coherent dynamics of both the crystal lattice and the electronic band energy can be directly measured by trXRD and trARPES, respectively. Focusing on the coherent lattice vibrations enables extracting phonon-mode-specific information with high precision. Conceptually, this is in analogy to electronic lock-in measurements, where a weak electronic signal is extracted by locking-in to a reference signal at the same frequency. Similarly, the light-induced coherent phonon mode provides an internal reference for measuring the EP coupling. 'Locking-in' on the phonon frequency avoids low-frequency contributions from other dynamical processes such as acoustic mode coupling or heat transport, which inevitably accompany optical excitation. As optical phonons in complex materials are in the THz regime, our approach brings this technique to the natural time scales of atoms and electrons, thus enabling deep insights into microscopic processes.

This coherent lock-in technique is ideal for studying the role of EP interactions in complex materials. In particular this applies to FeSe, which features strong correlation effects (*14*) as manifested by robust spin-fluctuations (*15–17*), a tendency toward nematic order (*17–19*), substantial orbital-dependent renormalization of the electron masses (*19,20*), and a non-monotonic pressure-dependence of the superconducting transition temperature (*21–23*). The capability to grow high-quality FeSe thin films by molecular beam epitaxy (*24*) enables implementation of advanced experiments.

We report an orbital-resolved coherent lock-in measurement of FeSe to quantify the EP coupling and assess the importance of electron correlations. Using a combination of trXRD and trARPES we detect lattice displacements at the sub-pm and band shifts at the meV level, respectively. Figure 1A depicts a schematic of the experiment, where a bulk-like 60 unit-cell thick FeSe film grown on $SrTiO_3$ is photo-excited by an ultrafast 1.5 eV infrared (IR) pump pulse. For trXRD, an 8.7 keV hard x-ray pulse tracks the photo-induced lattice dynamics at variable time delay Δt; for trARPES, a 6 eV ultraviolet (UV) pulse records the band energy dynamics (*25*). Benefiting from the single-mode response in FeSe, we lock-in to the coherent A_{1g} optical phonon (*26*), which corresponds to a periodic variation of the anion height (Fig. 1B, left inset) that has been shown to sensitively influence the electronic band structure (*9,27*), superconductivity (*23*) and antiferromagnetism (*10,28,29*) of iron-based materials.

Figure 1B shows the (004) Bragg intensity of the FeSe film measured by trXRD: upon photo-excitation ($\Delta t > 0$) the diffracted intensity is periodically modulated owing to the collective displacement of the selenium atoms. After subtracting a smoothed incoherent background, the coherent signal is well fit with an exponentially-decaying cosine (Fig. 1C). These data and the corresponding Fourier transforms (FT. Fig. 1B, right inset) demonstrate the cleanliness of the coherent response and exemplify the precision of our measurement, which allows resolving a 0.014 ± 0.003 THz hardening of the A_{1g} mode with decreasing temperature. Figure 1D shows that the coherent oscillation amplitude increases with increasing pump fluence, whereas the A_{1g} frequency does not noticeably change. The intensity change observed in trXRD is directly related to the coherent displacement $\delta z_{Se}(t)$ of the selenium atoms via a structure factor calculation ((*29*) and supplementary text) based on the symmetry of the A_{1g} phonon (Fig. 1E). We use

exponentially-decaying cosine fits with a linear background to extract the peak-to-peak amplitude Δz_{Se} at time zero.

To measure the impact of the coherent A_{1g} phonon on the electronic band structure, we have performed trARPES experiments. Photoemission spectra near the Brillouin zone center contain two prominent spectral features (Fig. 2A): 1) a hole-like band, which disperses between energies $E - E_F = 0$ and -100 meV, 2) a flat band located at $E - E_F \approx -200$ meV. E_F denotes the Fermi level. High-resolution equilibrium ARPES studies (*19,20*) have determined the orbital characters of the electronic bands near E_F using photon polarization selection rules. Comparison with these studies shows that the first and second band is of dominant $d_{xz/yz}$ and d_{z^2} orbital character, respectively. Electronic band dispersions calculated by density functional theory (DFT) are overlaid in Fig. 2A with an overall renormalization factor of 3, yielding good agreement with both the $d_{xz/yz}$ and d_{z^2} bands. Dashed lines denote bands that do not appear in trARPES, likely because of unfavorable photoemission matrix elements and the limited energy resolution.

The peak energies of the $d_{xz/yz}$ and d_{z^2} bands are extracted by fitting two Gaussians to constant-momentum cuts of the spectra (supplementary text). Figure 2B shows the $d_{xz/yz}$ band dispersions at an incident fluence $F = 0.62$ mJ/cm^2 and four representative delay times. At all momenta the band energy oscillates with the A_{1g} frequency of $f = 5.25 \pm 0.02$ THz. The extracted oscillation amplitudes exhibit a momentum dependence of up to 20% between $k_{||} = -0.22$ and -0.13Å^{-1}, yet this is comparable in magnitude to the overall uncertainties (supplementary text). Therefore, we average the energy dynamics within this momentum range, and display the averaged dynamics for the $d_{xz/yz}$ and d_{z^2} bands in Fig. 2C,D, respectively. We use exponentially-decaying cosine fits with a quadratic background to extract the peak-to-peak amplitudes ΔE at time zero.

Figure 3A compares the selenium displacement $\delta z_{Se}(t)$ extracted from trXRD to the energy dynamics of the two electronic bands $\langle E_{xz/yz}(t)\rangle$ and $\langle E_{z^2}(t)\rangle$ from trARPES. Time zero is independently determined in the two experiments, each yielding an uncertainty of ~20 fs. Within this accuracy, the lattice and electronic oscillations are synchronous: Both bands shift towards lower energy as the selenium atoms move away from the Fe planes (Fig. 3B). This correspondence is the same as that derived for the related compound $BaFe_2As_2$ (*29*).

The A_{1g} deformation potential near the Brillouin zone center is quantified by linear fitting of the fluence-dependent amplitudes Δz_{Se} and $\Delta E_{xz/yz,z^2}$ shown in Fig. 3C,D, respectively. We correct for the amplitude reduction caused by the finite time resolutions (supplementary text). Furthermore, for the calculation of the deformation potentials we include factors to account for the fluence averaging owing to finite pump and probe beam profiles, as well as, for the effective excitation densities per FeSe layer as determined by the pump and probe penetration depths (supplementary text). The fluence dependences indicate that both the trXRD and trARPES experiments sample a linear response, confirming that the coherent signal remains representative of the ground state. The coherent lock-in approach directly yields deformation potentials of $\Delta E_{xz/yz}/\Delta z_{Se} = -13.0 \pm 2.5$ and $E_{z^2}/\Delta z_{Se} = -16.5 \pm 3.2$ meV/pm.

The extracted EP deformation potentials allow a comparison to different theoretical approaches. Table 1 shows that canonical DFT, calculated in a non-magnetic state, underestimates the selenium height and overestimates the A_{1g} frequency. Moreover, the theoretical $d_{xz/yz}$ deformation potential is one order of magnitude smaller than in the experiment. In contrast, the calculated deformation potential of the d_{z^2} band is comparable to the experimental value within a factor of 2. The failure of DFT to reproduce these basic properties of FeSe (*5,15,30*) exemplifies the significant effect of electron correlations on the EP coupling.

Meanwhile, these properties can be quantitatively reproduced by incorporating electron-electron correlation effects via self-consistent density functional theory-dynamical mean field theory (DFT+DMFT) (*5,14*). For FeSe this approach (*5*) yields the correct band structure and selenium height, leading to a softer A_{1g} mode consistent with experiments (Tab. 1). In particular, Ref. (*5*) reported a band-averaged (maximum) A_{1g} deformation potential of $|\Delta E_{xz/yz}/\Delta z_{Se}|$ = 10.3 meV/pm (13.4 meV/pm) for the $d_{xz/yz}$ band—in agreement with our experimental value.

Our results differ from previous work (*10*) on $BaFe_2As_2$, which reported that the A_{1g} deformation potential obtained from DFT agrees adequately with experiments. We believe this discrepancy may be associated with the non-orbital-resolved nature of the comparison (*9,10*) and differences in the level of electron correlations in the two compounds (*14*). In contrast, our orbital-resolved lock-in experiment on FeSe establishes a clear case of significantly enhanced EP coupling in the presence of strong correlations.

Notably, the important role of correlation-enhanced EP coupling is not universally accepted, as most earlier work on Fe-based superconductors was focused on spin fluctuations without acknowledging the role of the EP coupling (*14-17,22*). Moreover, a direct experimental confirmation of the enhanced EP coupling strength has been lacking: phonon spectroscopies, such as Raman (*15*) and neutron scattering (*16,17*) lack orbital resolution, whereas photoemission (*7,19,20,24*) and tunneling (*8*) spectroscopy do not resolve phonons directly. Our method bridges this gap and measures all relevant degrees of freedom directly and allows us to test theories predicting the effect of correlations on the EP coupling.

In particular, FeSe exhibits a substantial and nontrivial increase of T_c from 8 to 37 K by application of pressure (*21–23*), which matches the pressure dependence of the EP deformation potential derived from DFT+DMFT (*5*), emphasizing that correlation effects have a strong

impact on superconductivity in FeSe. Moreover, the observation of a much-enhanced out-of-plane A_{1g} mode coupling, compared to DFT calculations (Tab. 1), suggests a small-momentum-transfer EP coupling, consistent with theoretical results on local EP interactions (*5*). Such a forward-scattering EP coupling likely interferes constructively with other electronic pairing channels (*24*), thereby providing a pathway towards superconducting states in which electron-phonon and electron-electron interactions act in concert.

The coherent lock-in approach establishes an experimental paradigm for precision measurements of fundamental physical quantities, such as the EP deformation potential, by only relying on a linear, coherent response. It provides a purely experimental and model-free technique that simultaneously yields complete information in time, space, momentum and energy with high sensitivity. Beyond the immediate implication that the 'renormalized' EP coupling strength in iron-based materials is considerably larger than anticipated by conventional theories, this approach also opens the window for unbiased tests of emergent phenomena in other controversial, correlated materials.

References and Notes:

1. D. C. Johnston. The puzzle of high temperature superconductivity in layered iron pnictides and chalcogenides. *Adv. Phys.* **59**, 803–1061 (2010).

2. O. Rösch, O Gunnarsson. Electron-phonon interaction in the *t-J* model. *Phys. Rev. Lett.* **92**, 146403 (2004).

3. A. S. Mishchenko, N. Nagaosa. Electron-phonon coupling and a polaron in the *t-J* model: from the weak to the strong coupling regime. *Phys. Rev. Lett.* **93**, 036402 (2004).

4. Z. P. Yin, A. Kutepov, G. Kotliar. Correlation-enhanced electron-phonon coupling: applications of GW and screened hybrid functional to bismuthates, chloronitrides, and other high-T_c superconductors. *Phys. Rev. X* **3**, 021011 (2013).

5. S. Mandal, R. E. Cohen, K. Haule. Strong pressure-dependent electron-phonon coupling in FeSe. *Phys. Rev. B* **89**, 220502(R) (2014).

6. J. Bardeen, L. N. Cooper, J. R. Schrieffer. Theory of superconductivity. *Phys. Rev.* **108**, 1175–1204 (1957).

7. A. A. Kordyuk *et al.* Angle-resolved photoemission spectroscopy of superconducting LiFeAs: evidence for strong electron-phonon coupling. *Phys. Rev. B* **83,** 134513 (2011).

8. D. Shimada, N. Tsuda, U. Paltzer, F. W. de Wette. Tunneling phonon structures and the calculated phonon density of states for $Bi_2Sr_2CaCu_2O_8$. *Physica C* **298**, 195–202 (1998).

9. L. X. Yang *et al*. Ultrafast modulation of the chemical potential in $BaFe_2As_2$ by coherent phonons. *Phys. Rev. Lett.* **112**, 207001 (2014).

10. L. Rettig, *et al.* Ultrafast structural dynamics of the Fe-pnictide parent compound $BaFe_2As_2$. *Phys. Rev. Lett.* **114**, 067402 (2015).

11. C. Bostedt *et al*. Linac Coherent Light Source: the first five years. *Rev. Mod. Phys.* **88**, 015007 (2016).

12. G. Grimvall. *The Electron-Phonon Interaction in Metals* (North-Holland Pub. Co., Amsterdam, 1981).

13. H. J. Zeiger *et al.* Theory for displacive excitation of coherent phonons. *Phys. Rev. B* **45**, 768–778 (1992).

14. Z. P. Yin, K. Haule, G. Kotliar. Kinetic frustration and the nature of the magnetic and paramagnetic states in iron pnictides and iron chalcogenides. *Nat. Mater*. **10**, 932–935 (2011).

15. V. Gnezdilov *et al*. Interplay between lattice and spin states degree of freedom in the FeSe superconductor: dynamic spin state instabilities. *Phys. Rev. B* **87**, 144508 (2013).

16. M. C. Rahn, R. A. Ewings, S. J. Sedlmaier, S. J., Clarke, A. T. Boothroyd. Strong (π,0) spin fluctuations in β-FeSe observed by neutron spectroscopy. *Phys. Rev. B* **91**, 180501(R) (2015).

17. Q. Wang *et al*. Strong interplay between stripe spin fluctuations, nematicity and superconductivity in FeSe. *Nat. Mater.* **15**, 159–163 (2016).

18. T. M. McQueen *et al.* Tetragonal-to-orthorhombic structural phase transition at 90 K in the superconductor $Fe_{1.01}Se$. *Phys. Rev. Lett.* **103**, 057002 (2009).

19. M. D. Watson *et al*. Emergence of the nematic electronic state in FeSe. *Phys. Rev. B* **91**, 155106 (2015).

20. A. Tamai *et al*. Strong electron correlations in the normal state of the iron-based $FeSe_{0.42}Te_{0.58}$ superconductor observed by angle-resolved photoemission spectroscopy. *Phys. Rev. Lett.* **104,** 097002 (2010).

21. S. Medvedev *et al.* Electronic and magnetic phase diagram of β-$Fe_{1.01}Se$ with superconductivity at 36.7 K under pressure. *Nat. Mater.* **8**, 630–633 (2009).

22. T. Imai, K. Ahilan, F. L. Ning, T. M. McQueen, R. J. Cava. Why does undoped FeSe become a high-T_c superconductor under pressure? *Phys. Rev. Lett.* **102**, 177005 (2009).

23. S. Margadonna *et al.* Pressure evolution of the low-temperature crystal structure and bonding of the superconductor FeSe (T_c = 37 K). *Phys. Rev. B* **80**, 064506 (2009).

24. J. J. Lee *et al*. Interfacial mode coupling as the origin of the enhancement of T_c in FeSe films on $SrTiO_3$. *Nature* **515**, 245–248 (2014).

25. Materials and methods are available as supplementary materials on *Science* Online.

26. S.-L. Yang *et al.* Thickness-dependent coherent phonon frequency in ultrathin FeSe/$SrTiO_3$ films. *Nano Lett.* **15**, 4150–4154 (2015).

27. I. Avigo *et al*. Coherent excitations and electron-phonon coupling in Ba/$EuFe_2As_2$ compounds investigated by femtosecond time- and angle-resolved photoemission spectroscopy. *J. Phys.: Con- dens. Matter* **25**, 094003 (2013).

28. K. W. Kim *et al.* Ultrafast transient generation of spin-density-wave order in the normal state of $BaFe_2As_2$ driven by coherent lattice vibrations. *Nat. Mater.* **11**, 497–501 (2012).

29. S. Gerber *et al.* Direct characterization of photoinduced lattice dynamics in $BaFe_2As_2$. *Nat. Commun.* **6**, 7377 (2015).

30. S. Margadonna *et al.* Crystal structure of the new $FeSe_{1-x}$ superconductor. *Chem. Commun.* 5607–5609 (2008).

31. M. Chollet *et al.* The X-ray Pump-Probe instrument at the Linac Coherent Light Source. *J. Synchrotron Rad.* **22**, 503–507 (2015).

32. D. Zhu, *et al*. Performance of a beam-multiplexing diamond crystal monochromator at the Linac Coherent Light Source. *Rev. Sci. Instrum.* **85**, 063106 (2014).

33. H. T. Lemke *et al.* Femtosecond optical/hard x-ray timing diagnostics at an FEL: implementation and performance. *Proc. of SPIE* **8778**, 87780S (2013).

34. P. Blaha, K. Schwarz, G. K. H. Madsen, D. Kvasnicka, J. Luitz. *WIEN2k, An Augmented Plane Wave + Local Orbitals Program for Calculating Crystal Properties* (Karlheinz Schwarz, Techn. Universität Wien, Austria, 2001).

35. J. P. Perdew, K. Burke, M. Ernzerhof. Generalized gradient approximation made simple. *Phys. Rev. Lett.* **77**, 3865–3868 (1996).

36. Z. Li *et al*. Structural and superconductivity study on α-$FeSe_x$. *J. Phys. Chem. Solids* **71**, 495–498 (2010).

37. P. Giannozzi *et al*. Quantum Espresso: a modular and open-source software project for quantum simulations of materials. *J. Phys.: Condens. Matter* **21**, 395502 (2009).

38. B. L. Henke, E. M. Gullikson, J. C. Davis. X-ray interactions: photoabsorption, scattering, transmission, and reflection at $E = 50 - 30,000$ eV, $Z = 1 - 92$. *At. Data Nucl. Data Tables* **54**, 181–342 (1993).

39. K. G. Nakamura, Y. Shikano, Y. Kayanuma. Influence of pulse width and detuning on coherent phonon generation. *Phys. Rev. B* **92**, 144304 (2015).

40. W. H. Richardson. Bayesian-based iterative method of image restoration. *J. Opt. Soc. Am.* **62**, 55–59 (1972).

41. L. B. Lucy. An iterative technique for the rectification of observed distributions. *Astron. J.* **79**, 745–754 (1974).

42. Reflectance of mirrors with protected silver coating. www.thorlabs.com/images/TabImages/Thorlabs_Protected_Silver_Coating.xlsx

43. M. Daimon and A. Masumura. High-accuracy measurements of the refractive index and its temperature coefficient of calcium fluoride in a wide wavelength range from 138 to 2326 nm. *Appl. Opt.* **41**, 5275–5281 (2002).

44. A. Damascelli, Z. Hussain, Z.-X. Shen. Angle-resolved photoemission studies of the cuprate superconductors. *Rev. Mod. Phys.* **75**, 473–541 (2003).

Acknowledgments: Use of the Linac Coherent Light Source (LCLS), SLAC National Accelerator Laboratory, is supported by the U.S. Department of Energy (DOE), Office of Science, Office of Basic Energy Sciences (BES) under contract DE-AC02-76SF00515. S.G., S.L.Y., H.S., J.A.S., S.R., J.J.L., T.J., B.M., C.J., A.G., Y.L., D.L., L.C., W.L., R.G.M., T.P.D., W.S.L., P.S.K., and Z.X.S. were supported by the DOE-BES Division of Materials Sciences and Engineering (DMSE) under Contract No. DE-AC02-76SF00515 (Stanford/SIMES). The authors gratefully acknowledge technical assistance at LCLS by D. Stefanescu and R. Fiebich. S.G. and D.L. acknowledge partial support by the Swiss National Science Foundation under fellowships P2EZP2_148737 and P300P2_151328, respectively. S.L.Y. acknowledges support by the Stanford Graduate Fellowship. H.S. acknowledges support from the Fulbright Scholar Program. A.G. acknowledges support by the National Defense Science & Engineering Graduate Fellowship Program. K.W.K was supported by Basic Science Research Program through the National Research Foundation of Korea funded by the Ministry of Science, ICT and future Planning (NRF-2015R1A2A1A10056200). Y.D.C. and Z.H. were supported by the Director, Office of Science, Office of Basic Energy Sciences, of the U.S. Department of Energy under contract No. DE-AC02-05CH11231. Raw data from the time-resolved x-ray scattering experiment is kept at the Linac Coherent Light Source of the SLAC National Accelerator

Laboratory. Time-resolved photoemission raw data is kept at the Shen Laboratory of Stanford University.

Supplementary Materials:

Materials and Methods

Supplementary Text

Figures S1–S12

Table S1

References (*31–44*)

Fig. 1. Experimental geometry and coherent lattice dynamics. (**A**) $FeSe/SrTiO_3$ films were measured by trXRD and trARPES. Δt denotes the delay of the x-ray (turquoise) and UV (purple) probe pulse with respect to the IR pump pulse (red). (**B**) X-ray intensity of the (004) Bragg peak as a function of Δt. Photo-excitation (F = 1.83 mJ/cm^2) initiates a coherent A_{1g} phonon (left inset), resulting in oscillations of the x-ray signal at the A_{1g} frequency (right inset). (**C**) Coherent x-ray signal at T = 20 K (blue) and 180 K (orange, raw data in Fig. S1) after subtracting a smooth background (black line in B). (**D**) Dependence of the x-ray signal on the incident fluence at T = 20 K. (**E**) Corresponding displacement δz_{Se}. Time zero was determined by the exponentially-decaying initial intensity drop (dotted black line in (D), convolved with the overall time resolution). Solid black lines indicate fits of the data. Errors denote 1 standard deviation obtained from the fitting. In (C), (D), and (E), curves are offset for clarity by the amounts indicated in each panel.

Fig. 2. Coherent electron dynamics. (**A**) Equilibrium photoemission spectrum at T = 20 K along the Γ-X direction. Electronic band dispersions calculated by DFT are overlaid (renormalized by a factor of 3). Dominant features correspond to one of the $d_{xz/yz}$ bands (orange) and the d_{z^2} band (blue). (**B**) Photo-induced shift of the $d_{xz/yz}$ band at four delays, corresponding to extrema of the coherent oscillations (denoted by vertical dashed lines in (C)). (**C** and **D**) Momentum-averaged energy shifts of the $d_{xz/yz}$ and d_{z^2} bands. Solid black lines indicate fits of the data. Traces in (C) and (D) are offset for clarity.

Fig. 3. Coherent 'lock-in' at the A_{1g} frequency. (**A**) Oscillations of the selenium displacement δz_{Se} (blue) and the momentum-averaged energy shift $\langle E_{xz/yz,z^2} \rangle$ (orange, green). trXRD and trARPES data were measured with F = 0.46 mJ/cm^2 and 0.37 mJ/cm^2, respectively. Black lines indicate fits of an exponentially-decaying cosine with a polynomial background to extract the peak-to-peak oscillation amplitudes Δz_{Se} and $\Delta E_{xz/yz,z^2}$ at time zero. (**B**) Schematic of the A_{1g} phonon mode (top), which periodically modulates the electronic band energies (bottom). (**C** and **D**) Lattice and band oscillation amplitudes as a function of the incident pump fluence. Solid lines indicate linear fits. Error bars in (C) and (D) denote statistical uncertainties, whereas the shaded areas represent systematic fluence uncertainties (supplementary text). The error of the fitted slopes accounts for both statistical and systematic uncertainties.

	Experiment	DFT+DMFT (*5*)	DFT
z_{Se} (r.l.u.)	0.2653	0.27	0.2456
f_{A1g} (THz)	5.30 ± 0.05	5.7	6.5 ± 0.3
$\Delta E_{xz/yz}/\Delta z_{Se}$ (meV/pm)	−13.0 ± 2.5	−10.3 to −13.4	−1.6 ± 0.2
$\Delta E_{z^2}/\Delta z_{Se}$ (meV/pm)	−16.5 ± 3.2	−	−8.5 ± 0.9

Tab. 1. Comparison of experiment and theory. Selenium height z_{Se}, A_{1g} phonon frequency f_{A1g}, as well as A_{1g} deformation potentials $\Delta E_{xz/yz}/\Delta z_{Se}$ and $\Delta E_{z^2}/\Delta z_{Se}$ obtained from experiments, canonical DFT calculations and DFT+DMFT by Mandal *et al.* (*5*) (band-average and maximum value). The experimental value for z_{Se} is taken from Margadonna *et al.* (*30*), whereas the deformation potentials are obtained by combining the data shown in Fig. 3C,D, and applying corrections for spatial integration over pump and probe profiles and effective energy densities (supplementary text). The error of the deformation potentials includes systematic and statistical uncertainties. DFT deformation potentials account for an empirical renormalization factor of 3 and the errors reflect the uncertainty of the renormalization determined from ARPES. Theoretical values for f_{A1g} are deduced from quadratic fits to the relative total energy.

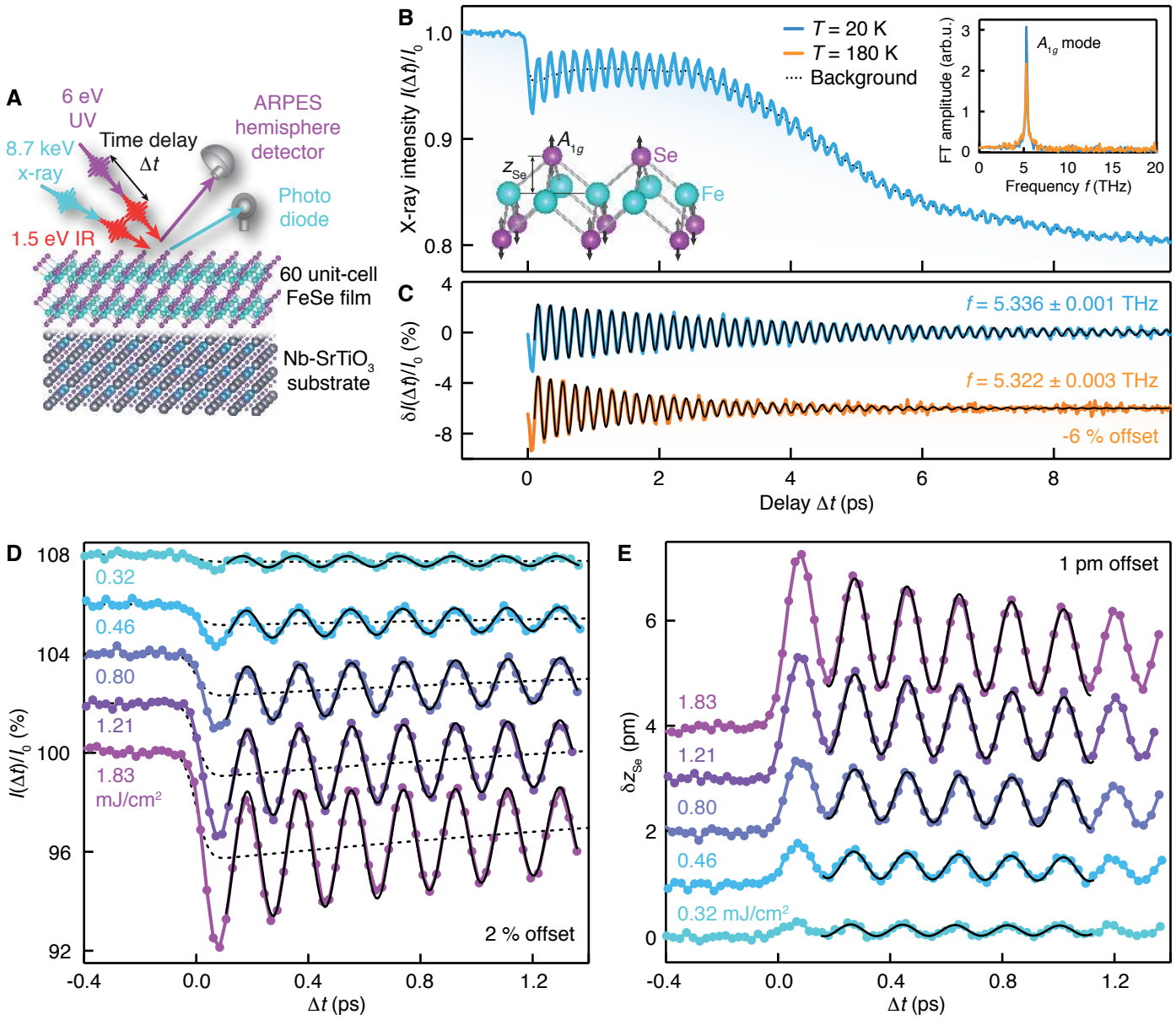
A
6 eV
UV
8.7 keV
x-ray
Time delay
Δt
ARPES
hemisphere
detector
Photo
diode
1.5 eV IR
60 unit-cell
FeSe film
Nb-SrTiO3
substrate
B
T = 20 K
T = 180 K
Background
X-ray intensity I(Δt)/I0
A1g
zSe
Se
Fe
FT amplitude (arb.u.)
A1g mode
Frequency f (THz)
C
δI(Δt)/I0 (%)
f = 5.336 ± 0.001 THz
f = 5.322 ± 0.003 THz
-6 % offset
Delay Δt (ps)
D
I(Δt)/I0 (%)
0.32
0.46
0.80
1.21
1.83
mJ/cm2
2 % offset
Δt (ps)
E
δzSe (pm)
1 pm offset
1.83
1.21
0.80
0.46
0.32 mJ/cm2
Δt (ps)

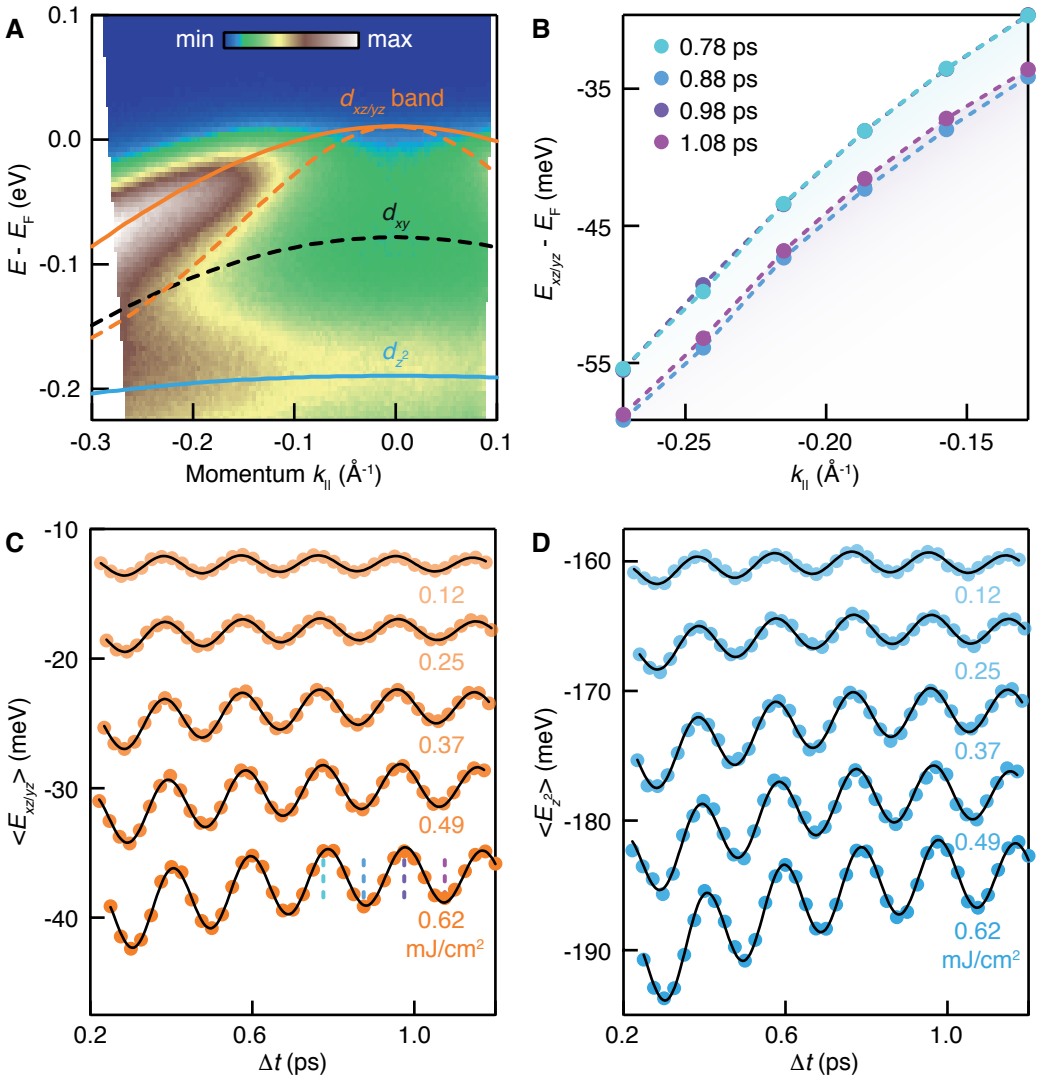
A
min
max
$d_{xz/yz}$ band
d_{xy}
d_{z^2}
E - E_F (eV)
Momentum $k_{||}$ (Å^{-1})
B
0.78 ps
0.88 ps
0.98 ps
1.08 ps
$E_{xz/yz}$ - E_F (meV)
$k_{||}$ (Å^{-1})
C
<$E_{xz/yz}$> (meV)
0.12
0.25
0.37
0.49
0.62
mJ/cm^2
Δt (ps)
D
<E_{z^2}> (meV)
0.12
0.25
0.37
0.49
0.62
mJ/cm^2
Δt (ps)

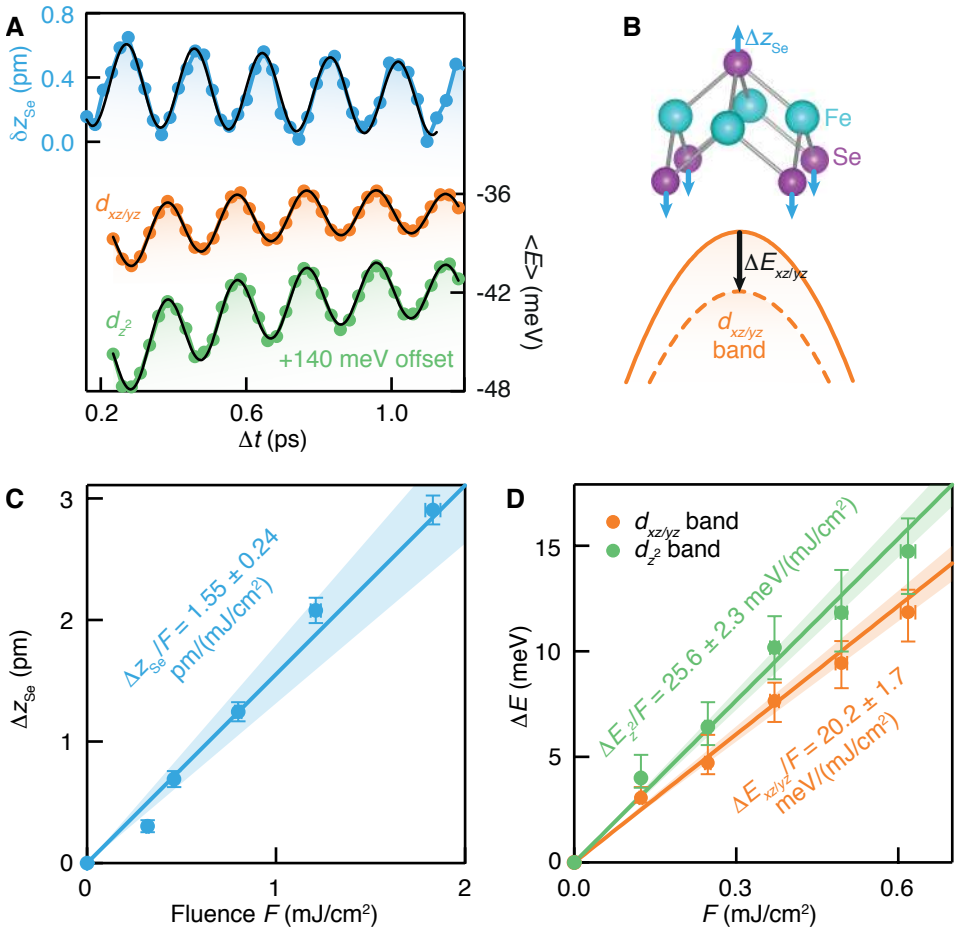
A
0.8
0.4
0.0
δz_{Se} (pm)
$d_{xz/yz}$
d_{z^2}
+140 meV offset
-36
-42
-48
<E> (meV)
0.2
0.6
1.0
Δt (ps)
B
Δz_{Se}
Fe
Se
$\Delta E_{xz/yz}$
$d_{xz/yz}$ band
C
3
2
1
0
Δz_{Se} (pm)
$\Delta z_{Se}/F$ = 1.55 ± 0.24 pm/(mJ/cm²)
0
1
2
Fluence F (mJ/cm²)
D
$d_{xz/yz}$ band
d_{z^2} band
15
10
5
0
ΔE (meV)
$\Delta E_{z^2}/F$ = 25.6 ± 2.3 meV/(mJ/cm²)
$\Delta E_{xz/yz}/F$ = 20.2 ± 1.7 meV/(mJ/cm²)
0.0
0.3
0.6
F (mJ/cm²)